Acta Geotechnica
https://doi.org/10.1007/s11440-020-01007-6

RESEARCH PAPER

Modeling the mechanical behavior of coarse-grained soil using additive manufactured particle analogs

Sheikh Sharif Ahmed[1] · Alejandro Martinez[1]

Received: 22 November 2019 / Accepted: 16 June 2020

Abstract
Systematic investigation of the effects of individual particle properties, such as shape, size, surface roughness, and constituent materials stiffness, on the behavior of coarse-grained soils requires careful control over the other particle properties. Achieving this control is a pervasive challenge in investigations with naturally occurring soils. The rapid advance of modern additive manufacturing (AM) technology provides the ability to create analog particles with independent control over particle size and shape. This work evaluates the feasibility of the stereolithography (SLA) and polyjet technologies to generate analog particles that can model the mechanical behavior of coarse-grained soils. AM is used to generate equal-sized spheres and analog sand particles from 3D X-ray CT scans of natural rounded and angular sand particles. The uniaxial inter-particle compression, oedometer compression, and shear wave transmission behaviors of the AM particles are investigated and compared to those of glass and steel spheres and natural rounded and angular sand particles. The results indicate that AM can successfully reproduce the shape of natural coarse sand particles. The deformation of micro-asperities was found to influence the contact response of the polyjet AM particles, thus affecting their inter-particle uniaxial compression and oedometer compression response. The contact response of the SLA AM particles was closer to that of glass spheres. Both AM particle types exhibit a dependency of shear wave velocity and shear modulus on mean effective stress that is consistent with that of natural sands.

Keywords Additive manufacturing · Granular materials · Inter-particle compression · Shear stiffness · Soil analog · 1D compression · 3D printing

1 Introduction

Skeletal forces transmitted at the particle–particle contacts resulting from applied boundary stresses control the mechanical behavior of coarse-grained soil [43]. The inherent properties of the particles, such as their shape, size, surface roughness, and the stiffness of their constituent materials, control the normal and shear deformation response of the contacts. These particle-scale interactions govern the global-scale response observed in both laboratory and field tests.

Several researchers have examined the effects of different inherent particle properties on the engineering properties of coarse-grained soils, such as the friction angle, shear wave velocity, and small-strain shear modulus, often reporting contradicting trends. In triaxial compression tests on specimens of uniformly graded sand and glass beads, Kirkpatrick [31] and Marschi et al. [34] observed an increase in both friction angle (ϕ') and dilatancy with a decrease in particle size. On the contrary, an increase in ϕ' with an increase in particle size has also been reported based on direct shear test results [26, 30, 47, 49]. Xiao et al. [51] observed an increase in both peak and critical state friction angles with a decrease in particle regularity at a given confining stress from triaxial compression tests. Casini et al. [9] also observed similar trends from direct shear tests. Contradictory observations on the effects that particle size and shape have on the shear wave velocity (V_s) and small-strain modulus (G_{max}) of coarse-grained soils

✉ Alejandro Martinez
amart@ucdavis.edu

Sheikh Sharif Ahmed
ssah@ucdavis.edu

[1] University of California Davis, Davis, USA

Published online: 28 June 2020

have also been reported in the literature. For instance, Patel et al. [42] and Bartake and Singh [6] reported that the V_s of sand increases as the mean particle size (D_{50}) decreases. In contrast, Iwasaki and Tatsuoka [27], Wichtmann and Triantafyllidis [50], and Yang and Gu [53] observed no significant effect of D_{50} on V_s, whereas Sharifipour et al. [45] and Bui [7] reported an increase in V_s with increasing D_{50}. Iwasaki and Tatsuoka [27] reported no significant influence of particle shape on G_{max}. In contrast, an increase in G_{max} has been reported with both increasing particle roundness (i.e. decreasing angularity) by Bui [7] and Cho et al. [15] and decreasing particle roundness by Altuhafi et al. [3] and Liu and Yang [33]. These types of contradictory observations likely result from the pervasive challenge to experimentally control individual particle properties in natural soils.

Additive manufacturing (AM) or 3D printing technology has advanced rapidly in the last decade. This technology can be used to generate artificial soil analogs with independent control over particle size, shape, and gradation [1, 23]. In recent years, researchers have used AM technology to generate particles of different sizes and shapes [1, 5, 23, 36]. A morphological comparison study conducted by Adamidis et al. [1] on Hostun sand particles and AM analogs showed that these analogs can successfully replicate the morphology of natural particles. Authors have also performed triaxial tests on specimens of AM particles of different shapes and sizes [1, 5, 36]. Some of these results show that the assemblies of AM particles exhibit stress–dilatancy behavior similar to that typical of frictional granular materials [1, 23, 35]. Other studies have revealed that AM particles qualitatively exhibit key aspects of 1D compression behavior of natural soils, such as differences in the compression and recompression indices [22]. These findings qualitatively suggest that AM particle analogs can emulate the macroscale behavior of coarse-grained soil.

Despite the similarities in mechanical behavior of assemblies composed of natural and additive manufactured particles, further insight requires the understanding of inter-particle contact behavior, which depends on particle morphology as well as the mechanical properties of the particle constituent material [10]. The force–displacement response of particle contacts under compression indicates a transition from an approximately linear relationship at lower forces to a Hertzian response at higher forces [10–12, 17, 18]. The threshold force at which the behavior changes depends on the particle morphology and material stiffness [10]. Kittu et al. [32] characterized the contact behavior of AM spheres of two different materials and showed that the Hertzian behavior is observed after a threshold force and suggest that AM materials can feasibly be used for applications such as validation of discrete element modeling (DEM) simulations.

The current study presents a methodology to generate additive manufactured particles with similar size and morphology to natural soil particles. Three behaviors of these AM particles are then investigated: inter-particle uniaxial compression, oedometric compression of assemblies, and shear wave transmission and small-strain shear moduli of assemblies. For each behavior investigation, the response of the AM particles is compared to that of particles and specimens of glass and stainless-steel spheres and rounded and angular natural sand particles.

2 Inter-particle contact response

Hertz theory describes the force–deformation relationship for two elastic spheres in contact. The contact stress is a function of the applied normal force (F), particle radii ($R_{1,2}$), Young's moduli ($E_{1,2}$), and Poisson's ratios ($v_{1,2}$) of the spheres. According to Hertz theory, the contact deformation, δ, can be calculated as:

$$\delta = \left(\frac{9}{16}\frac{F^2}{RE^{*2}}\right)^{1/3} \tag{1}$$

where R is the effective radius of curvature expressed as: $1/R = 1/R_1 + 1/R_2$, and E^* is the effective Young's modulus defined as: $1/E^* = \left(1 - v_1^2\right)/E_1 + \left(1 - v_2^2\right)/E_2$.

Hertz theory assumes that the strains are small and elastic, the surfaces of the bodies are continuous and nonconforming, each body can be considered as elastic half-space, the surfaces are frictionless, and the contact is non-adhesive. Prior research shows that the normal force–displacement response of two spheres pressed against each other usually follows the behavior predicted by Hertz theory within a certain force interval. Antonyuk et al. [4] describe four stages of the force–displacement relationship as shown in Fig. 1: (I) plastic deformation of micro-asperities on the contact surface, (II) elastic deformation predicted by Hertz theory, (III) elasto-plastic deformation, and (IV) breakage.

Initial plastic response due to the deformation of micro-asperities was reported by Cavarretta et al. [10], who observed plastic yielding (stage I in Fig. 1) until the contact normal force F reached a threshold force, N_{GT}. The threshold force depends on the particle's surface roughness, surface radius at the contact point, and Young's modulus [20]. Once F exceeds N_{GT}, the force–displacement response follows that predicted by Hertz theory (stage II in Fig. 1). Point N in Fig. 1 represents a transition between stage II and stage III, where elastic deformations give way to plastic yielding and deformations accumulate at a larger rate than predicted by

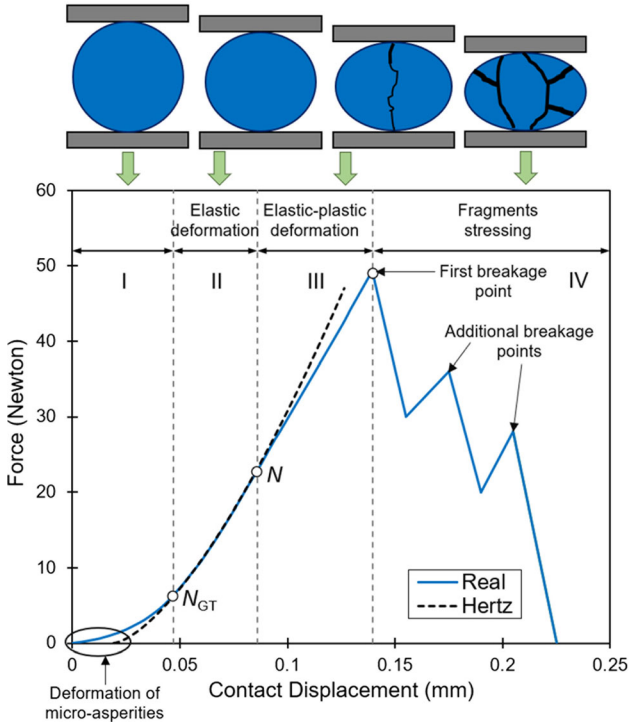

Fig. 1 Typical contact force–displacement curve up to failure (redrawn after Antonyuk et al. [4])

Hertz theory. With further increase in force, the *first breakage point* is reached and the particle begins to suffer significant breakage as shown in stage IV.

3 Hertz-based normalization of contact deformation

Important insight into the small- and medium-strain behavior of coarse-grained soil can be achieved with elastic contact mechanics theories, such as Hertz theory [43]. Development of an interpretation framework based on Hertz theory would thus capture the stage II behaviors shown in Fig. 1, which is described with the particle's Young's modulus and size.

For a contact between spheres of the same material to undergo the same deformation as another contact composed of spheres of different radii and constituent materials, the following condition must be met:

$$\left(\frac{F_1^2}{R_1 E_1^{*2}}\right)^{1/3} = \left(\frac{F_2^2}{R_2 E_2^{*2}}\right)^{1/3} \tag{2}$$

The average normal force at inter-particle contacts in an assembly of mono-sized spheres with a random packing is related to the effective stress within the assembly (σ'), radius of the spheres (R), and void ratio of the assembly (e) [43], as follows:

$$F = C\sigma' R^2 \tag{3}$$

where C is a coefficient that describes the particle tributary area and can be expressed as $C = \pi(1+e)^{2/3}$ [43]. Considering assemblies of particles to undergo the same average contact deformation, Eq. 2 can be written as:

$$\left[\frac{C_1 \sigma_1' R_1}{E_1^{*2}}\right]^{1/3} = \left[\frac{C_2 \sigma_2' R_2}{E_2^{*2}}\right]^{1/3} \tag{4}$$

For assemblies with the same void ratio and particle size, Eqs. 2 and 4 lead to the following relationship:

$$\frac{F_1}{E_1^*} = \frac{F_2}{E_2^*} \quad \text{or} \quad \frac{\sigma_1'}{E_1^*} = \frac{\sigma_2'}{E_2^*} \tag{5}$$

This relationship indicates that the same average deformation will be experienced at the particle contacts if the ratio of the contact force to the constituent material's Young's modulus is equal for the two assemblies. For assemblies, an additional requirement of an equal void ratio must also be met.

Figure 2a shows the Hertzian force–displacement relationship for contacts between particles composed of steel, glass, and polymer. The curves correspond to equal-sized spheres with a diameter of 3.175 mm and show that a greater force is required to obtain a given deformation for contacts between particles with higher Young's modulus. Figure 2b presents curves in terms of normalized force (F/E^*) for the same materials. The three curves overlap, indicating that the normalized force required to produce a given contact deformation is independent of the Young's modulus. This normalization, however, ignores plastic deformation of micro-asperities and contact yielding.

4 Materials and methods

Experiments were performed on eight different types of particles to characterize their contact- and element-scale responses. This section describes the AM technology employed in this investigation, the materials tested, and the experimental procedures used to characterize their mechanical response.

4.1 Additive manufacturing technology

Advances in AM technology have developed different methods and materials that enable modern 3D printers to generate objects with a wide range of precision and cost. Large-scale, specialized 3D printers can generate highly complex geometries using materials such as metals, polymers, ceramics, and concrete with high accuracy. Some of those printers can mix different materials on demand to

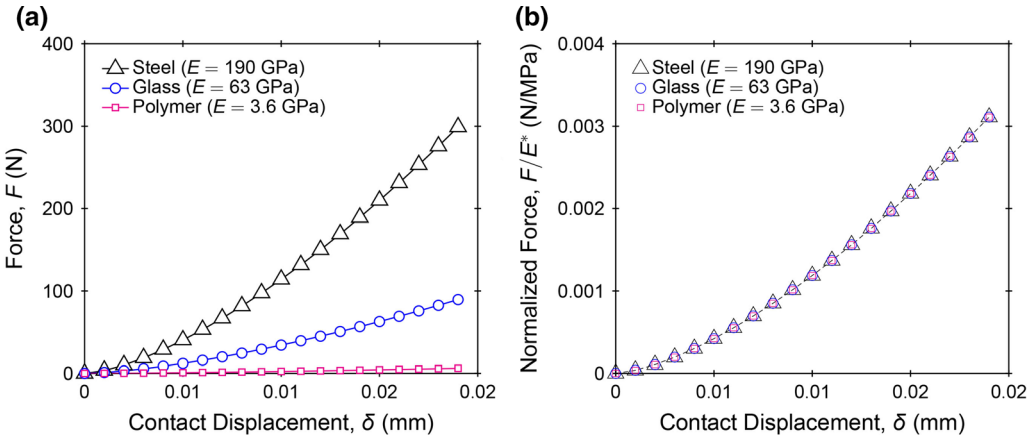

Fig. 2 Hertzian relationships for steel, glass, and polymer particle contacts in terms of **a** contact force versus displacement and **b** normalized contact force versus displacement

achieve desired mechanical properties [28, 39]. Desktop 3D printers are typically constrained to printing polymers; however, even these printers can print layers with thickness in the order of 10 to 30 μm [40]. These fast-paced advances offer design freedom and production flexibility which have established 3D printers as a conventional tool in many science and engineering research laboratories [46].

Different AM methods provide certain advantages and drawbacks. The stereolithography (SLA) and polyjet AM methods are popular in research and prototyping to manufacture small, detailed parts because they are relatively inexpensive and quick [1, 23, 32]. Hence, this study uses these two AM methods to evaluate differences in the responses of the manufactured AM particles and their implications in modeling of coarse-grained soil behavior. Stereolithography uses an ultraviolet (UV) laser to cure and harden thin layers of liquid photopolymer resin contained in a reservoir (Fig. 3a). After a layer solidifies, the build platform moves up by a distance equivalent to one layer, and this process is repeated to produce a 3D object. A support structure attached to the printed object prevents deflection and warping. After printing and washing the object with alcohol to clean off uncured resin from its surface, the support structure is removed by cutting and the printed object further cures under UV light at temperatures between 40° and 80 °C to increase the polymer stiffness and strength. The second method considered here is the polyjet technology, which also uses a UV laser to harden liquid photopolymer resin (Fig. 3b). However, polyjet printers have two print heads that deposit different resins, where one resin creates the desired object, while the other resin acts as the support structure. The support structure is then removed from the finished 3D object either by water jetting or treatment using a 2% sodium hydroxide solution.

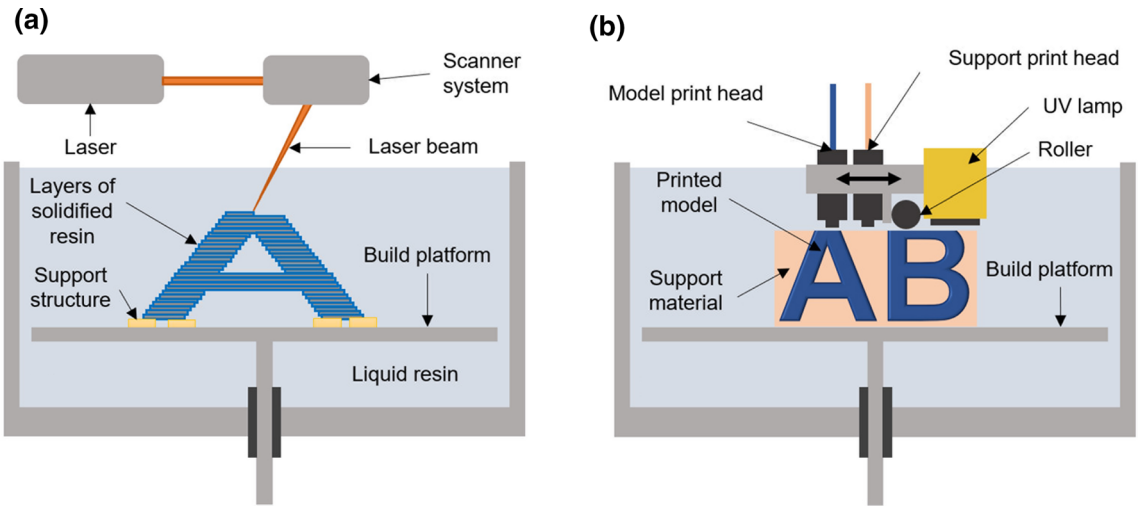

Fig. 3 Schematics of additive manufacturing technologies used to generate the spheres and particle analogs: **a** stereolithography (SLA) and **b** polyjet

4.2 Equal-sized spheres

This study examined eight different particle types (Fig. 4). Four types were spheres with a diameter of 3.175 mm composed of 304 stainless steel, borosilicate glass, SLA photopolymer, and polyjet acrylate-based polymer. Table 1 lists selected properties of these materials. The SLA spheres were generated using a *Form 2* printer from Formlabs with clear photopolymer resin (FKGPCL02). The print layer thickness was 25 μm, requiring a total of 127 layers to print one sphere. The polyjet spheres were generated using an *Objet Eden 260 V* printer from Stratasys with *VeroWhitePlus* rigid acrylate-based polymer resin with a printing resolution of 30 μm.

Figure 5 shows X-ray CT scans of the SLA and polyjet spheres. Both the direction of the SLA sphere layers and the asperity left by the support structure are visible. The scans also show that the polyjet spheres have a greater surface roughness compared to the SLA spheres. Table 1 includes the measured angle of repose (ϕ_{rep}) of all the spheres. Results indicate that the glass spheres have the smallest ϕ_{rep}, whereas the polyjet spheres have the largest ϕ_{rep}. Since all the spheres have the same particle shape and size, the differences in ϕ_{rep} suggest that the glass spheres have the smallest surface roughness and the polyjet spheres have the largest surface roughness. The specific gravity values indicate that steel is the densest material and both 3D printing resins are the least dense materials.

Table 1 Properties of the experimental materials

Material	Young's modulus, E (GPa)	Poisson's ratio, v	Specific gravity, G_s	Angle of repose*, ϕ_{rep} (°)	N_{GT} (N)
Steel spheres	190[a]	0.30[a]	7.82[a]	26.3	–
Glass spheres	63[a]	0.20[b]	2.23[a]	23.4	4
SLA 3DP spheres	3.6[a]	0.27[c]	1.15[f]	27.3	6
Polyjet 3DP spheres	2.4[a]	0.30[d]	1.18[f]	31.8	12
Quartz (angular)	76[e]	0.31[e]	2.65[e]	36.3	–
Quartz (rounded)	76[e]	0.31[e]	2.65[e]	32.2	–
Polyjet 3DP (angular)	2.4	0.30	1.18	39.2	–
Polyjet 3DP (rounded)	2.4	0.30	1.18	36.5	–

[a]Material specification sheet

[b]Otsubo et al. [41]

[c]Kittu et al. [32]

[d]Assumed

[e]Santamarina et al. [44]

[f]Measured in laboratory

*Measured using the method by Miura et al. [38]

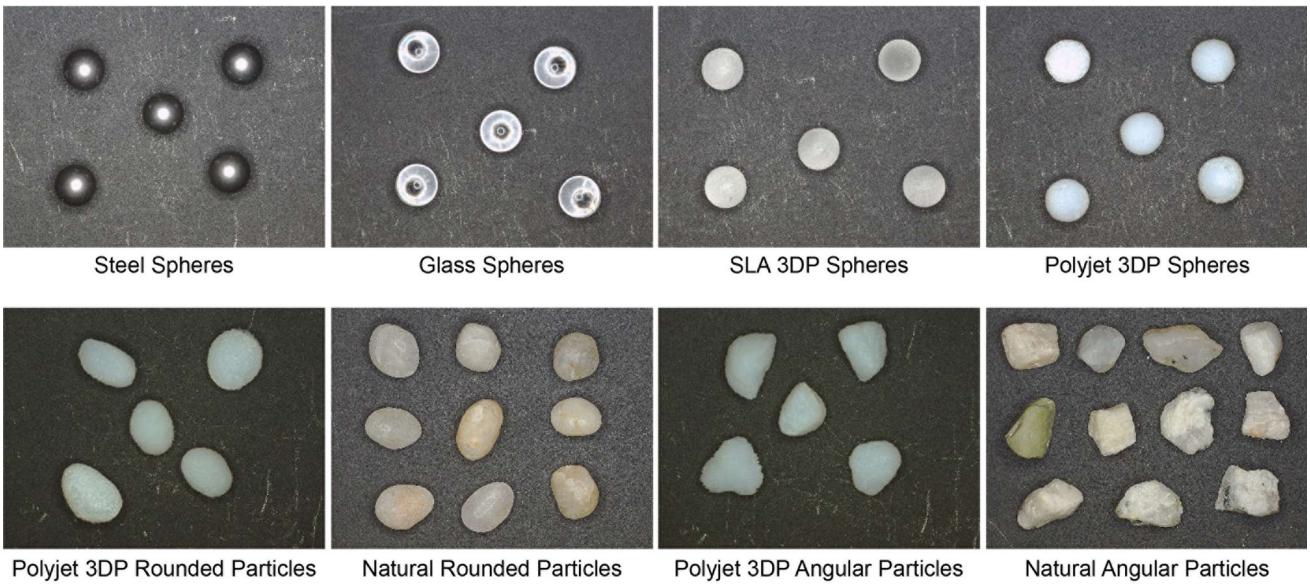

Fig. 4 Spherical, angular, and rounded particles of different materials used in this study

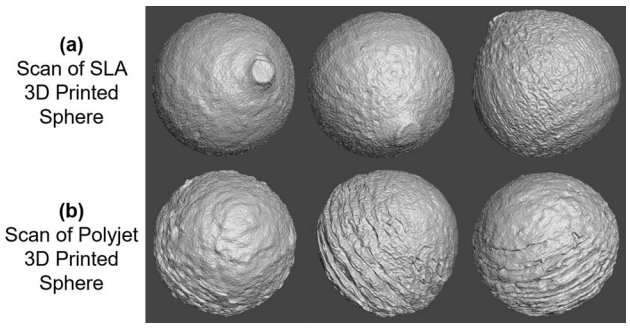

Fig. 5 X-ray CT scans of additive manufactured spheres: **a** SLA and **b** polyjet

4.3 Natural and additive manufactured sand particles

Natural quartz particles were separated by sieving a well-graded sand to obtain samples passing through the #6 (3.36 mm) and retained by the #8 (2.38 mm) sieves. This resulted in a poorly graded sandy soil composed of both angular and rounded particles. The particles were then manually separated to create two sand samples: one with angular particles and one with rounded particles (Fig. 4). This methodology offers the advantage of ensuring that both natural sand samples have the same gradation and mineralogy and only differ in particle morphology. To generate the additive manufactured particle analogs, 90 angular and 70 rounded natural sand particles were first chosen randomly for X-ray CT scanning with a resolution of 10 μm (Fig. 6a). These scans were reduced in resolution to increase the speed of the AM process (Fig. 6b), which were used to generate the analog particles using the polyjet technology (Fig. 6c). The AM particles appear significantly rougher than the natural particles due to the polyjet printing procedure. The influence of the larger surface roughness can be appreciated in the ϕ_{rep} measurements, with consistently larger values for both angular and rounded analog particles than for the natural particles.

The similarity between the natural and additive manufactured particles was assessed through comparison of particle morphology. Typically, roundness and sphericity are used to quantify particle shape. Roundness is a measure of the sharpness of a particle's edges and corners, whereas sphericity is a measure of the similarity of the particle shape to a circle or sphere. The roundness of a particle is defined as the ratio of the average radius of curvature of the particle corners to the radius of the largest inscribed circle [48]. The sphericity of a particle can be defined in a number of ways [21, 37]; here, the following parameters were considered: *area sphericity* (ratio of the projected area of a particle to the area of the minimum circumscribing circle), *perimeter sphericity* (ratio of the perimeter of the particle to the perimeter of a circle having the same projected area as the particle), and *width-to-length ratio*. The shape parameters were obtained from image analysis of photographs of particles using the code by Zheng and Hryciw [55]. As Fig. 7 shows, all the shape parameters of the AM particle analogs compare well with those of the natural particles, indicating that morphology is successfully reproduced.

4.4 Particle–particle compression test

A uniaxial compression loading frame was built to characterize the normal contact force–displacement behavior of spherical particles. Figure 8a shows a schematic of the testing setup, which consists of two custom-made pedestals fabricated with 316 stainless steel and two 18-8 stainless-steel holders, each of which has a machined 3.185 mm diameter circular hole. The spheres were attached to the holes with ethyl cyanoacrylate glue. An electric actuator

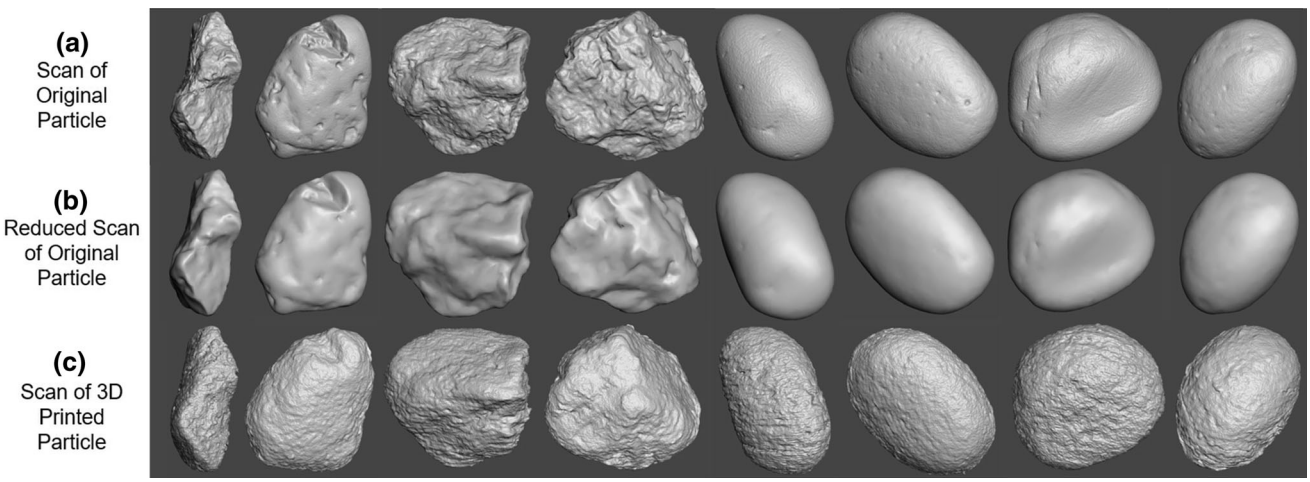

Fig. 6 Comparison of X-ray CT scans of **a** natural particles, **b** reduced scans for 3D printing, and **c** of additive manufactured particle analogs

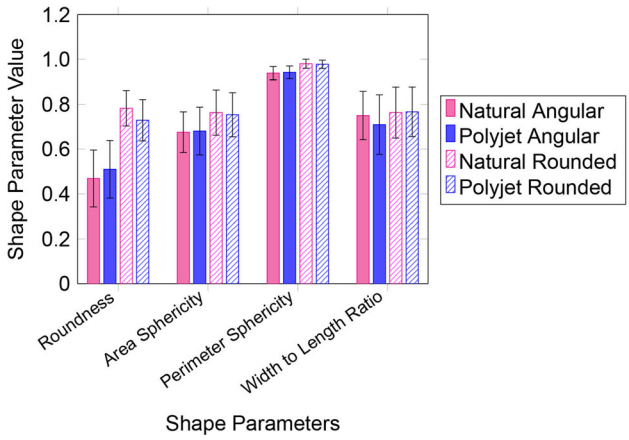

Fig. 7 Comparison of shape parameters for natural and additive manufactured particles (*Note*: standard deviation shown by error bars)

was used to apply the displacement-controlled compression. Three linear variable differential transformers (LVDT) with a range of ± 1.27 mm were used to measure the contact displacement. The LVDTs were attached to the top pedestal with three custom-made aluminum clamps, and differences in the readings were used to identify any tilting of the particles during testing. Two different load cells with capacities of 100 N and 1000 N were used to measure the applied load on the SLA and polyjet particles, and glass and steel particles, respectively. An initial investigation indicated no significant effect of the displacement rate on the force–displacement response for values between 0.03 and 0.003 mm/s. Thus, a displacement rate of 0.003 mm/s was used in all tests. The force–displacement response for the steel, glass, SLA, and polyjet spheres was measured with three cycles of subsequently increasing load. Load levels applied to the different materials were determined so that the normalized force, F/E^*, was 0.008 N/MPa for glass and steel and 0.06 N/MPa for the SLA and polyjet polymers.

4.5 Oedometer compression test

One-dimensional oedometer compression tests were performed on assemblies of spheres and sand (natural and AM) particles to characterize their stress–strain response. Figure 8b shows a schematic of the oedometer testing setup. A custom-made mold made of 316 stainless steel with an inside diameter and height of 63.5 mm was used to contain the specimens. An electric actuator was used to apply displacement-controlled compression at a rate of 0.02 mm/s to each specimen. Vertical displacements were measured with an LVDT, and the load was measured with a load cell. Specimens were prepared by pouring the particles in the testing mold in three lifts. After pouring each lift, the specimen side was tapped with a rubber mallet to densify the specimen to its target void ratio. Specimens were prepared at initial void ratios of 0.55 ± 0.02, 0.60 ± 0.02, and 0.65 ± 0.02 for all materials except the glass spheres, as their maximum attainable void ratio was 0.60. The maximum applied normalized vertical stress (σ'_v/E^*) was 4×10^{-5} for all the specimens, which was selected based on experience to prevent breakage or significant yielding of the particle contacts according to Ahmed et al. [2].

4.6 Bender element test

The small-strain response of spherical and sand (natural and AM) particle assemblies was examined by means of bender element tests. Figure 8c shows a schematic of the bender element test setup. Specimens with a diameter of 70 mm and a height between 58 and 70 mm were contained within a latex membrane. Bender elements with

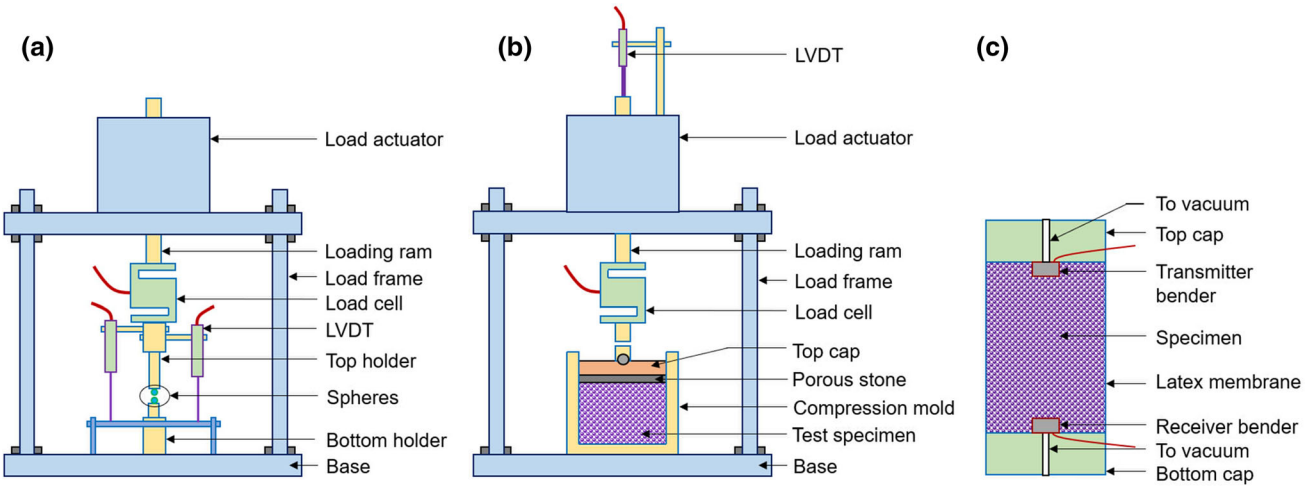

Fig. 8 Schematics of devices for **a** uniaxial particle–particle compression, **b** oedometer compression, and **c** bender element tests

12.7 mm in length, 8 mm in width, and 0.66 mm in thickness were attached to the top and bottom caps, which were used to send and receive the *S*-waves. The shear wave velocity was calculated using the travel time from the transmitter to the receiver bender. The wave arrival time was taken as the initial rise of the signal, defined as the time when a signal first crossed the *x*-axis, as described by Yamashita et al. [52]. Shear wave velocity measurements were obtained for specimens with initial void ratios of 0.55 ± 0.02, 0.60 ± 0.02, and 0.65 ± 0.02. The specimens were prepared following the same procedure as stated above. Isotropic confining pressures between 10 and 70 kPa were applied to all the specimens using a vacuum pump.

5 Results

This section presents results from the uniaxial particle–particle compression, oedometer compression, and bender element tests aimed at characterizing the behavior of the additive manufactured particles and comparing it to that of other particle types. Individual particle tests provide information about the contact response, whereas tests on assemblies enable an evaluation of the element-level stress–strain and stiffness behavior.

5.1 Uniaxial particle–particle compression

The contact force–displacement response of equal-sized spheres of stainless steel, glass, SLA polymer, and polyjet polymer was investigated. Figure 9 provides force–displacement results for each material, along with the response predicted by Hertz theory. Figure 10 presents results in terms of the normalized contact force (F/E^*) and the force ratio (F/N_{GT}). Although five tests were conducted for each material, the results of only one representative test are shown here for brevity.

The contact force–displacement response of the glass and SLA spheres is mostly elastic at lower loads, as shown in Fig. 9. The threshold force (N_{GT}) is about 4 N for the glass spheres and about 6 N for the SLA spheres. The response of the glass spheres begins to deviate from the Hertz prediction at a normal force (F) of about 30 N, corresponding to an F/E^* of about 0.0009 N/MPa (Fig. 10a) and an F/N_{GT} of about 7.5 (Fig. 10b). Deviation from the Hertz prediction begins at about 20 N for the SLA particles, corresponding to an F/E^* of about 0.01 N/MPa (Fig. 10c) and an F/N_{GT} of 3.4 (Fig. 10d). The contact plastic deformation (δ_{pm}) after unloading is significantly lower for the glass spheres than for the SLA particles (Fig. 10b, d), indicating that the SLA spheres underwent a larger amount of plastic deformation either due to deformation of micro-asperities or contact yielding. However, under a similar applied normalized contact force, both the glass and SLA 3D printed spheres have similar contact displacements (Fig. 10a). The plastic deformation of micro-asperities (i.e., stage I in Fig. 1) is strongly pronounced in the response of the polyjet AM particles, as shown in Fig. 9d, where the second dotted line represents the Hertz solution with a constant offset in the initial constant displacement. For these particles, N_{GT} has a magnitude of about 12 N. After stage I, the force–displacement response is somewhat elastic as predicted by Hertz theory as shown in the offset Hertzian relationships in Fig. 10a e, f. However, the response begins to deviate from the Hertz theory at a normal force of about 22 N, corresponding to an F/E^* of 0.017 N/MPa. The polyjet spheres exhibit a higher δ_{pm} than the glass and SLA spheres. In addition, under similar applied F/E^*, the polyjet contact displacement is higher than that for glass and SLA due to the larger deformations accumulated during stage I. The steel spheres exhibited yielding starting from a very small normal force of about 10 N ($F/E^* \approx 0.0001$ N/MPa). The stage I regime (i.e., plastic deformation of micro-asperities) and stage III regime (i.e., elasto-plastic deformation) appear to govern the force–displacement response, resulting in a large deviation from the Hertzian prediction, in accordance with Goldsmith and Lyman and Kagami et al. [19, 29].

5.2 Oedometer compression

Results from the 1D oedometer compression tests highlight the effects of constituent material stiffness on the compression response of particle assemblies. Figure 11 shows the results of spherical particle tests in terms of vertical strain ($\Delta H/H_0$) versus effective vertical stress (σ'_v) for specimens with e_0 of 0.55, 0.60, and 0.65. Results of two tests per material are presented here denoted by 'Test 1' and 'Test 2' in the legend (Fig. 11). Both types of AM sphere specimens require the lowest stress to achieve a certain vertical strain, followed by the glass spheres and then by the steel spheres with the highest stress, as shown in Fig. 11a–c, due to differences in Young's moduli where $E_{polyjet} < E_{SLA} < E_{glass} < E_{steel}$. The assemblies of polyjet spheres are more compressible than the other assemblies for all e_0 and especially appreciable for $e_0 = 0.65$. In terms of normalized stress (σ'_v/E^*), the compression responses of all the specimens aggregate in a tighter band as depicted in Fig. 11d–f. However, the curves for both the AM spheres lie to the right of the curves for the steel and glass spheres. The results indicate that the Hertz-based normalization does not account for other effects that influence the compression behavior of granular assemblies, such as yielding of micro-asperities and plastic yielding at particle contacts

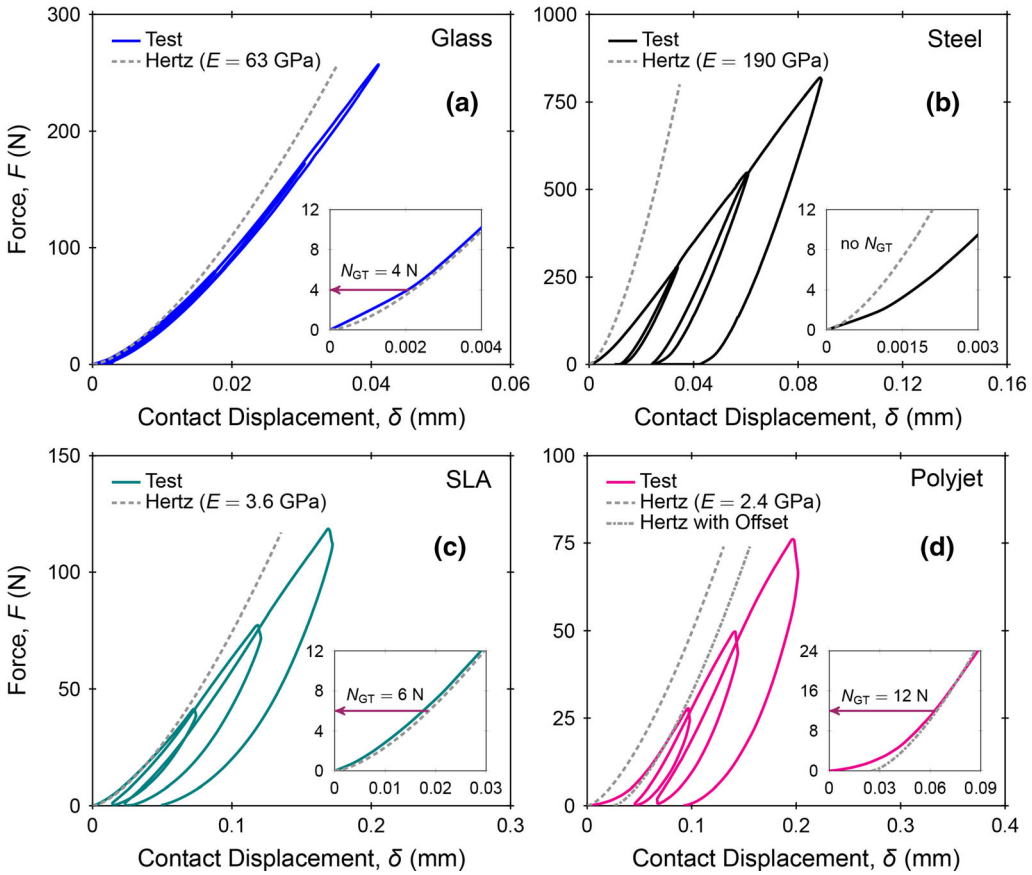

Fig. 9 Force–displacement response from uniaxial particle–particle compression tests for spheres of **a** glass, **b** steel, **c** SLA 3D printing resin, and **d** polyjet 3D printing resin

(stages I and III in Fig. 1). The compression curves collapse to a more compact band when plotted using a modified normalization, as shown in Fig. 11g–i, where the Young's modulus is raised to an empirically determined power $n = 0.70$ as follows:

$$\frac{\sigma'_{v1}}{E_1^{*0.7}} = \frac{\sigma'_{v2}}{E_2^{*0.7}} \tag{6}$$

Similar to the observation in Fig. 11, the specimens of additive manufactured angular and rounded sand particles require a lower stress to undergo a given amount of vertical strain than the specimens of natural sand, as shown in Figs. 12a–c and 13a–c, respectively. The compression curves aggregate in a tighter band when plotted in terms of normalized stress using Eq. 6 (Figs. 12d–f, 13d–f), although the polyjet assemblies of both angular and rounded particles are more compressible than the natural particles at larger normalized stresses.

Differences in compressibility for the specimens of different constituent materials but of similar particle shape and void ratio can be due to different amounts of either contact plastic deformation or particle rearrangement. Ahmed et al. [2] investigated the distribution of contact normal forces within an assembly of spheres with an $e_0 = 0.60$ using 3D discrete element modeling simulations. The authors found that for an applied normalized stress of $\sigma'_v/E^* = 4 \times 10^{-5}$, the average and 95th percentile contact forces were 20 N and 62 N for assemblies of glass spheres, respectively, and 1.0 N and 3.5 N for assemblies of polyjet polymer, respectively. Comparing these values to the results from uniaxial particle compression tests suggests the contact forces in the glass sphere assemblies largely remain in the elastic regime (stage II in Fig. 1) bounded by an N_{GT} of about 4 N and an onset of contact yielding of about 30 N. On the other hand, the contact forces in the polyjet sphere assemblies remain in the micro-asperity yielding regime (stage I in Fig. 1), where $F < N_{GT}$, with an N_{GT} of about 12 N. This comparison indicates that the larger compressibility of the polyjet assemblies is likely due to the larger initial compressibility of the rougher interparticle contacts.

All sphere assemblies exhibit larger compression indices (C_c) as e_0 is increased, as shown in Fig. 14a, likely due to the larger contact forces transferred at the contacts and more pronounced rearrangement of particles with increasing σ'_v. The polyjet spheres exhibit higher C_c at each e_0

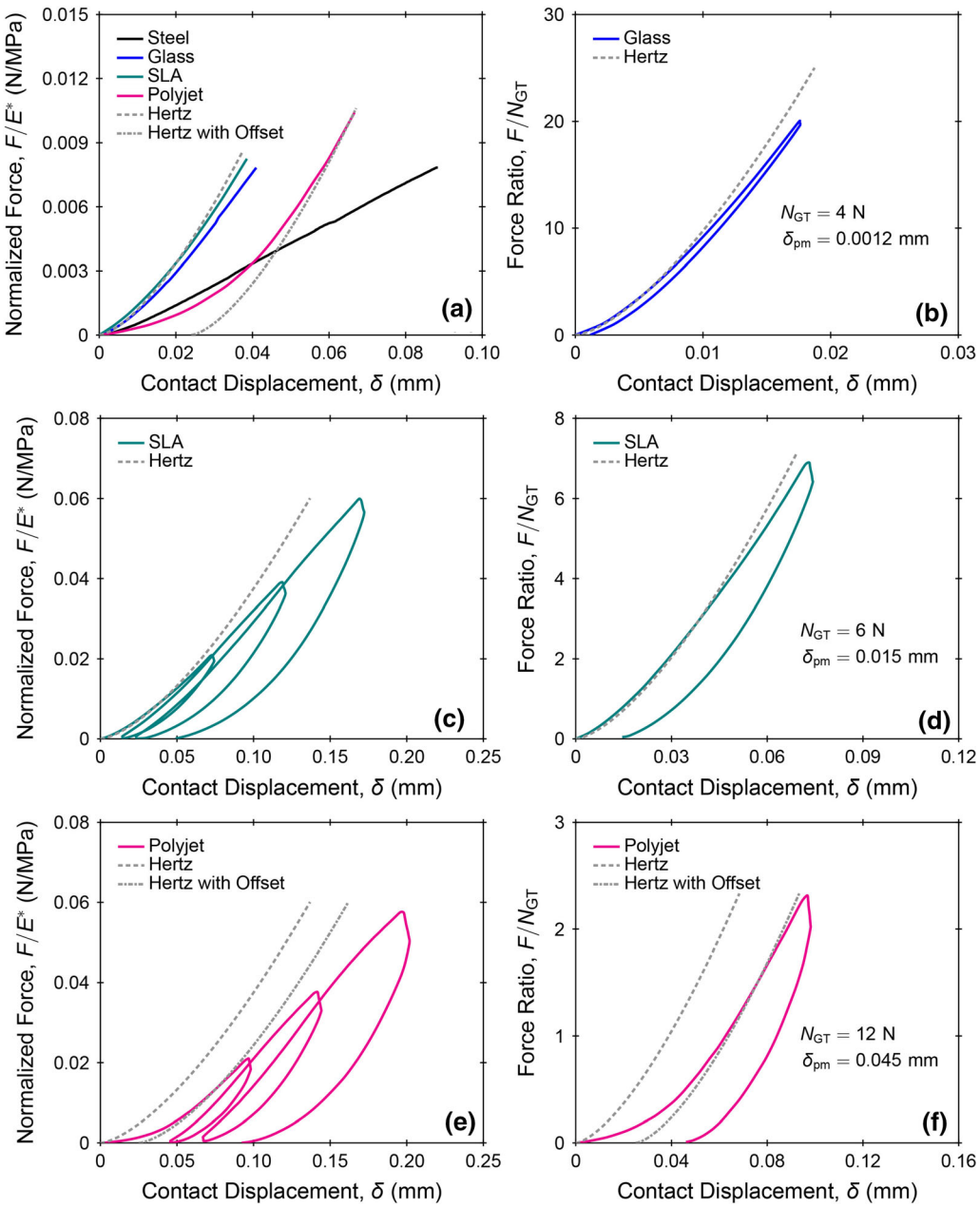

Fig. 10 Normalized force (F/E^*)–displacement response for **a** all spheres, **c** SLA AM spheres and **e** polyjet AM spheres and force ratio ($F/$FGT)–displacement plots for **b** glass spheres, **d** SLA AM spheres, and **f** polyjet AM spheres

compared to the other sphere types. Figure 14b shows that C_c values for the SLA, glass, and steel specimens are relatively independent of the constituent material Young's modulus (E). Figure 14c shows that, similar to the spherical particles, the natural particles and 3D printed analogs exhibit higher C_c as e_0 is increased, although C_c is systematically larger for the polyjet specimens. In addition, the rounded particle specimens have a slightly larger compressibility than the angular particle specimens for both natural and AM particles. These results indicate that while the AM analogs can qualitatively model the compression behavior of natural soils, some AM materials and processes, such as polyjet, can result in exaggeration of certain behaviors such as 1D compression.

5.3 Shear wave velocity and small-strain modulus

The shear wave velocity (V_s) for assemblies of spheres and sand (natural and AM) particles was obtained using bender elements. The corresponding shear moduli or small-strain moduli (G_{max}) were then determined using the relationship

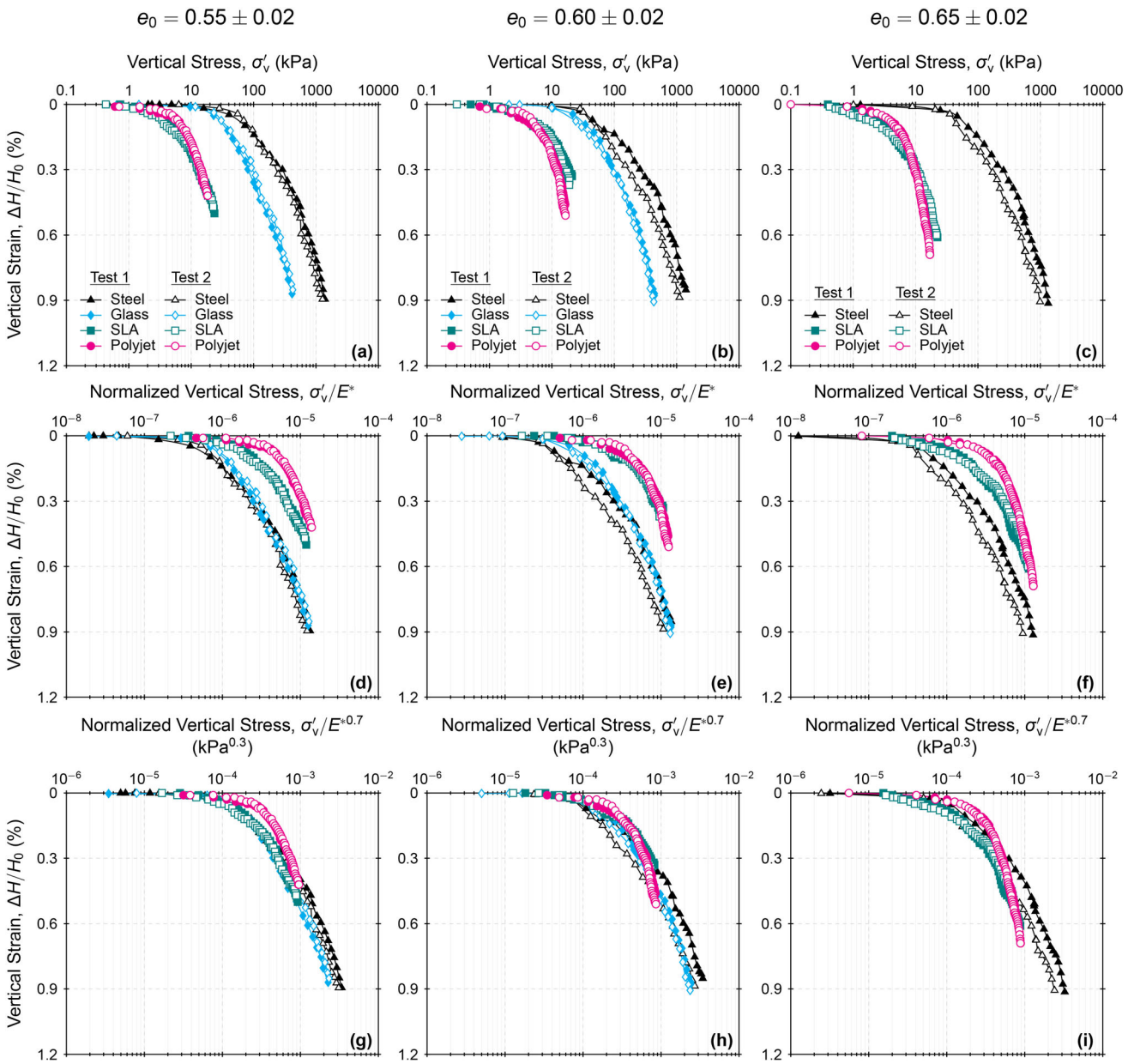

Fig. 11 Oedometric compression test results for spheres: **a**, **b**, **c** strain versus stress, **d**, **e**, **f** strain versus normalized stress (σ'_v/E_*), and **g**, **h**, **i** strain versus normalized stress ($\sigma'_v/E_*^{0.7}$)

$G_{max} = \rho V_s^2$, where ρ is the specimen density. Figure 15 shows typical transmitter and receiver bender signals for glass and polyjet sphere assemblies at different isotropic stresses.

The effect of the constituent material stiffness on the shear wave velocity is examined through V_s measurements on specimens of steel, glass, SLA, and polyjet spheres with similar initial void ratio (e_0), as shown in Fig. 16a–c. The V_s decreases as e_0 is increased for any given p'. The steel spheres exhibit higher V_s for all e_0 compared to the glass and AM spheres due to the steel's larger stiffness. The SLA and polyjet specimens have similar V_s values, which are greater than those for glass. Since the particle shape and void ratio are similar between the specimens, the likely cause of higher V_s in the AM specimens relative to the glass specimens is a larger inter-particle contact area facilitated by the softer polymer material, especially considering the high surface roughness that leads to significant plastic contact deformation.

A comparison of the V_s measurements on specimens of angular and rounded natural and AM particles shows similar trends as the tests on spheres, where V_s decreases as e_0 is increased for both the natural and analog particles (Fig. 16d–f). The AM particles exhibit a higher V_s

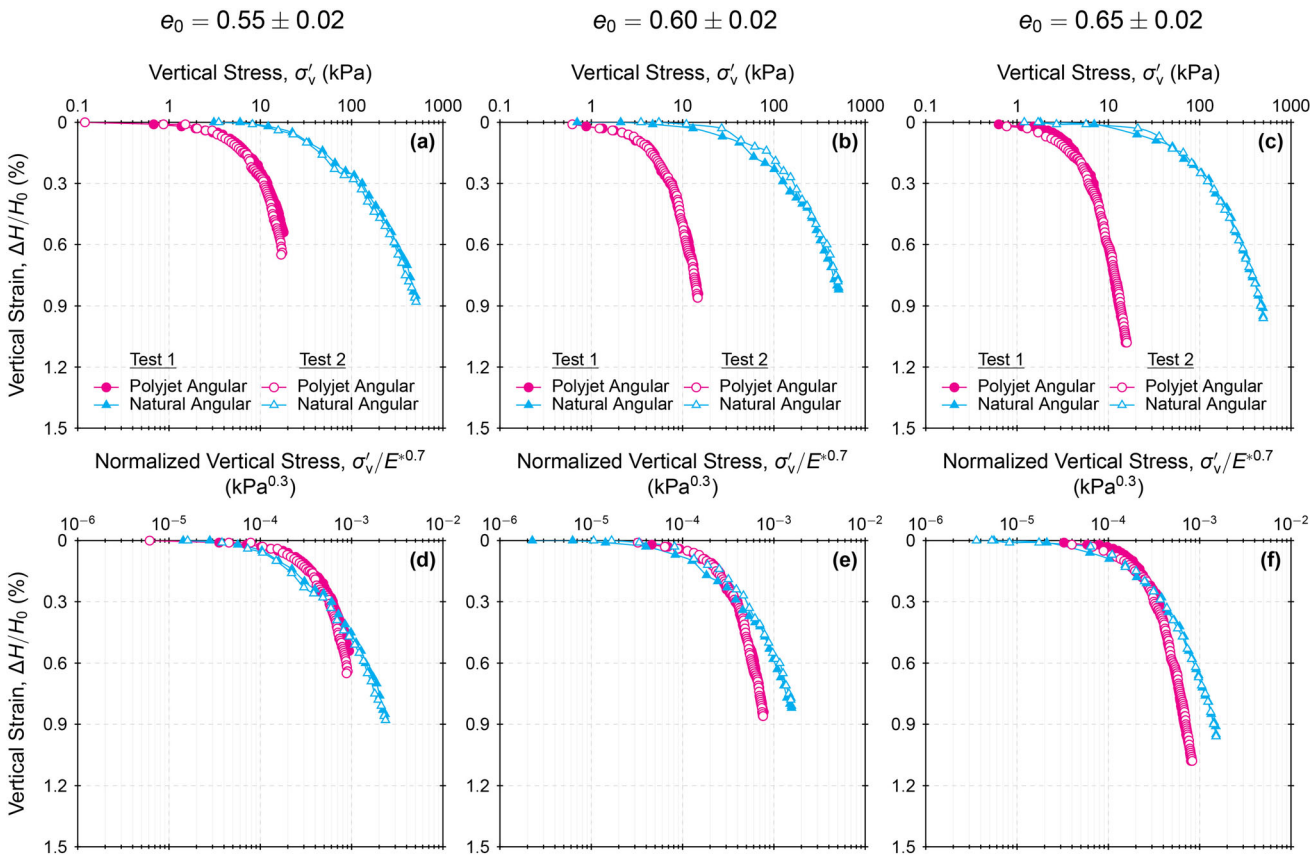

Fig. 12 Oedometric compression test results for angular natural and additive manufactured particles: **a**, **b**, **c** strain versus stress and **d**, **e**, **f** strain versus normalized stress ($\sigma'_v/E_*^{0.7}$)

compared to the natural particles; similarly, the AM spheres have larger V_s measurements than the glass spheres. The rounded particles exhibit slightly larger V_s values than the angular particles for both natural and 3D printed specimens, consistent with trends reported in the literature [15].

The shear wave velocities for the AM materials are larger during unloading than during loading for any given p, as shown in Fig. 17a, c, d. The polyjet spheres display a stronger difference than the SLA spheres, which is likely due to the larger plastic contact deformation as observed in the uniaxial particle–particle compression tests. This greater deformation leads to a larger contact area, which increases the stiffness of the contact. The V_s measured on assemblies of glass and steel, as shown in Fig. 17b, indicates that the values are only slightly larger during unloading than during loading, suggesting a small amount of contact plastic deformation. The sand particle tests reveal similar trends, with significantly larger V_s values measured during unloading for the polyjet specimens and almost similar values measured during loading and unloading for the natural sand specimens.

A comparison of the dependency of the shear wave velocity on the mean effective stress for the different materials can be made based on a power-law equation of the following form:

$$V_s = \alpha(p')^{\beta} \tag{7}$$

where α is the shear wave velocity (m/s) at an effective stress of 1 kPa and β reflects the evolution of the contacts' stiffness as a function of mean effective stress [13]. The values of α-coefficients and β-exponents of all the specimens were obtained from fitted relationships as shown in Fig. 16. Figure 18a, b provides the α- and β-values for specimens composed of spheres and sand particles, respectively. As the void ratio is decreased, the α-coefficient generally increases and the β-exponent generally decreases. For the tests on spheres, the α-coefficients are similar for the SLA and polyjet specimens and higher for the steel specimens. The α-coefficients obtained from sand specimens indicate slightly larger values for the polyjet particles than for the natural particles (Fig. 18b). The values of the β-exponents for the sphere specimens range between 0.1553 and 0.1913. For these tests, the β–exponent generally decreases with increasing constituent material

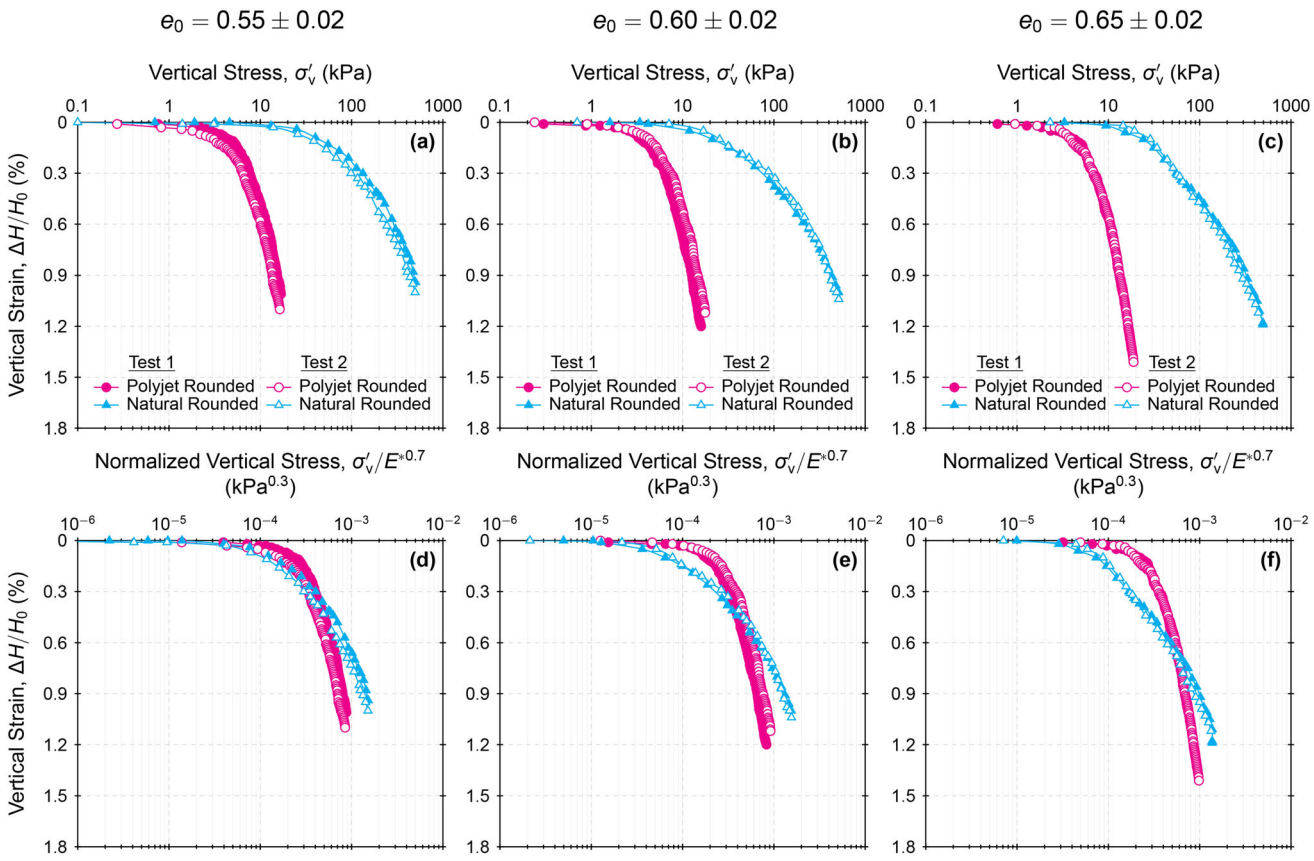

Fig. 13 Oedometric compression test results for rounded natural and additive manufactured particles: **a**, **b**, **c** strain versus stress and **d**, **e**, **f** strain versus normalized stress ($\sigma'_v/E_*^{0.7}$)

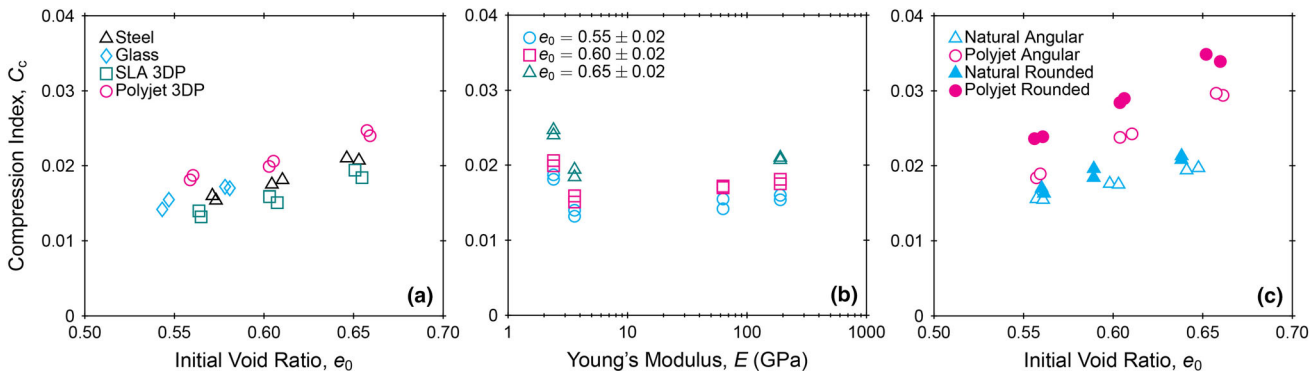

Fig. 14 Compressibility indices from oedometric compression tests: **a** C_c versus e_0 for spheres, **b** C_c versus E for spheres and **c** C_c versus e_0 for additive manufactured and natural sand particles

stiffness such that steel has the lowest values and the AM polymers have the larger values. The β-exponents for the natural and analog sand specimens range between 0.2060 and 0.2480, and the values for the AM specimens are generally slightly higher than those for the natural particle specimens at any given initial void ratio.

As indicated by Cascante and Santamarina [8], the β-exponent values can range between 0 and 0.75 depending on the type of contact (e.g., curved or cone-to-plane) and contact response (e.g., Hertzian elastic or elasto-plastic). Theoretical β-values for Hertzian inter-sphere contacts (i.e., stage II in Fig. 1) are equal to 0.167 and for elastic cone-to-plane contacts and spheres experiencing contact yield are equal to 0.25 [8]. Since the β-exponents obtained from the test results on sphere specimens are generally larger than 0.167, they indicate that the contacts do not exhibit a pure Hertzian response possibly due to contact yielding and particle rearrangement. This effect is more

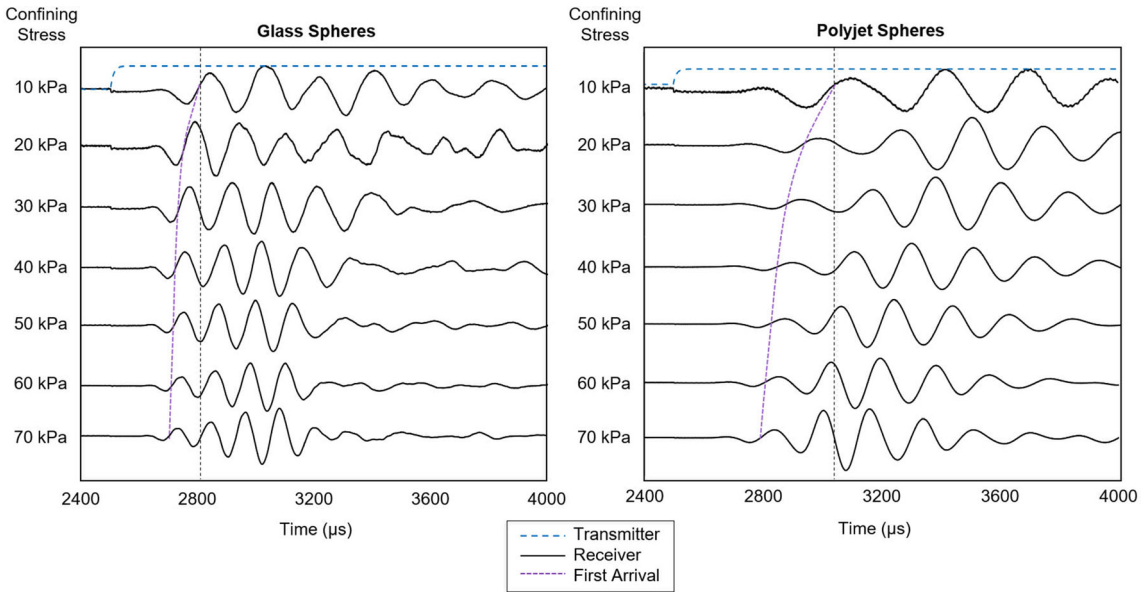

Fig. 15 Receiver bender element signals for glass and polyjet spheres at different isotropic stresses. Note that the initial height of glass sphere specimen was 59.7 mm, whereas the initial height of polyjet sphere specimen was 68.6 mm

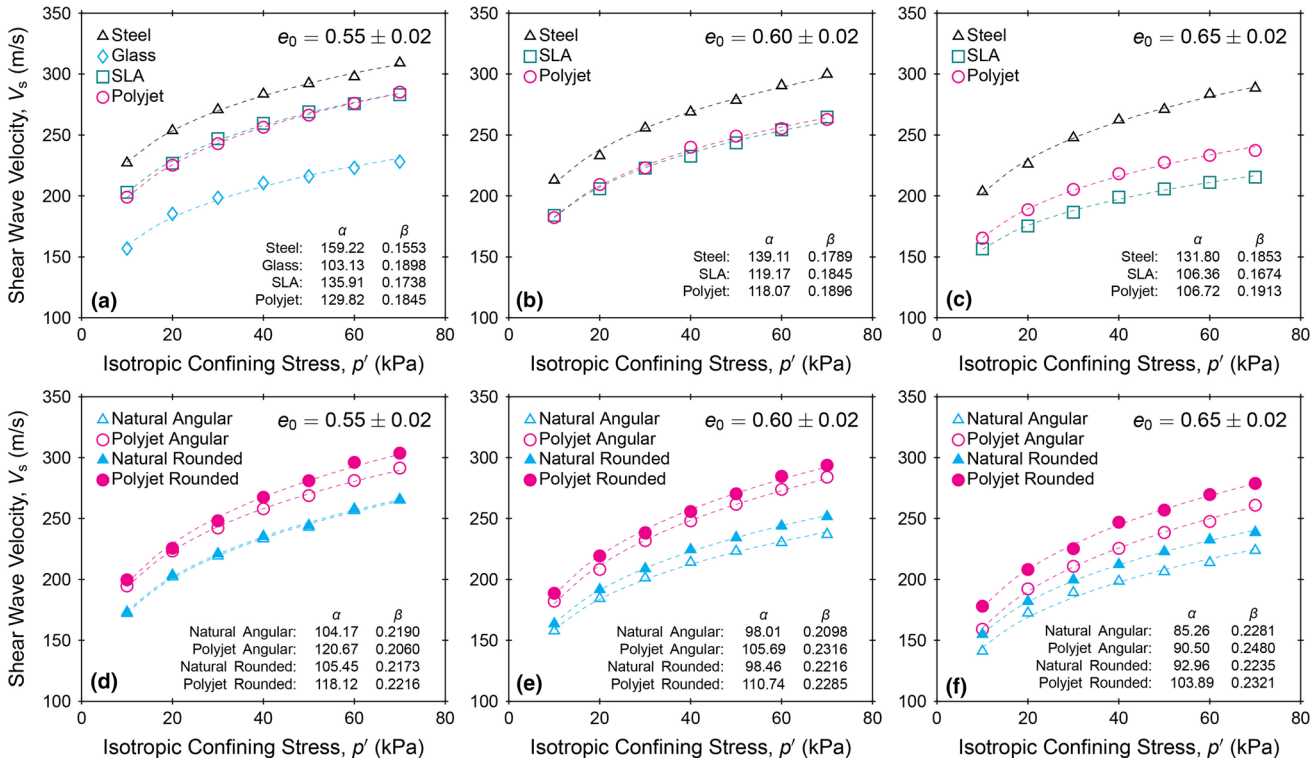

Fig. 16 Shear wave velocities for specimens of **a**, **b**, **c** spheres and **d**, **e**, **f** natural and polyjet angular and rounded particles

pronounced for the natural and analog sand particles, which yielded larger β-exponents in agreement with trends reported in the literature [13]. Figure 18c presents a comparison of α- and β-values of the specimens of natural and AM sand particles with those from natural sands reported by Cha et al. [13]. As shown, the values from this investigation are within the range for sands reported in the literature, suggesting that the AM analogs can reproduce the relationship between V_s and p' for coarse-grained soils.

The small-strain shear moduli (G_{max}) of the spherical particles specimens show similar trends, where G_{max} increases with decreasing e_0 and increasing p' (Fig. 19a–c).

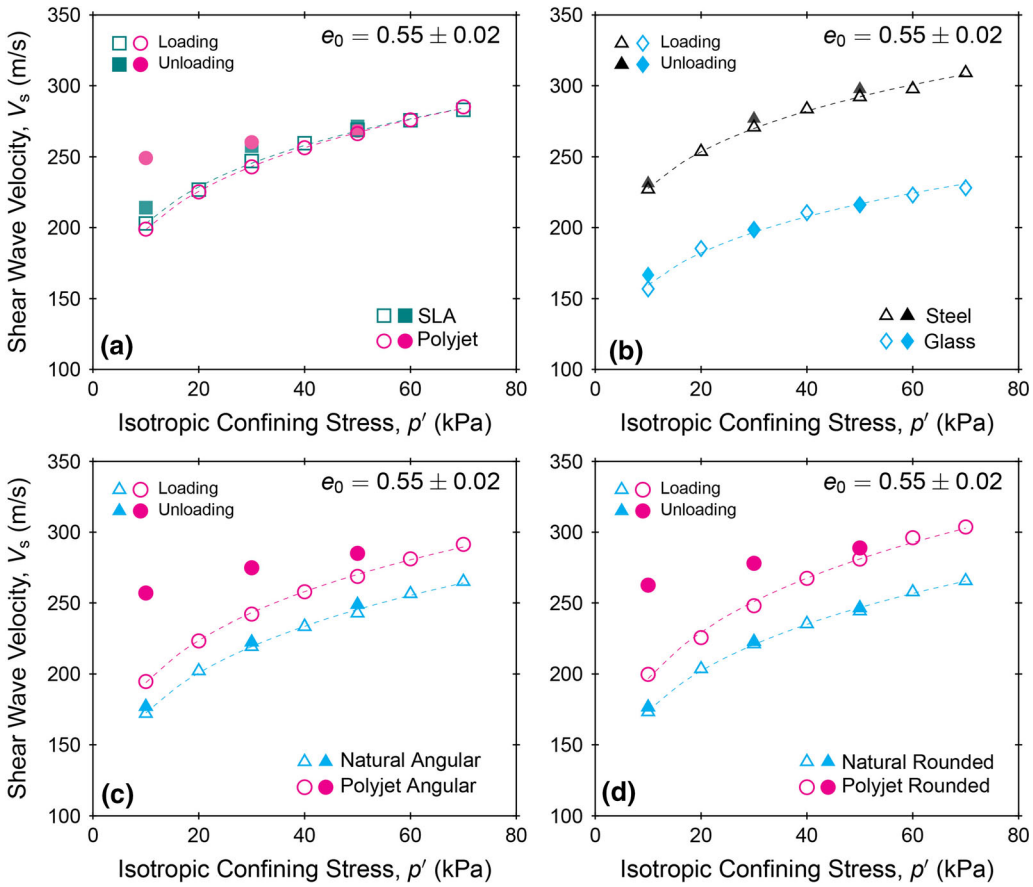

Fig. 17 Shear wave velocities during loading and unloading for **a**, **b** spheres and **c**, **d** natural and polyjet angular particles

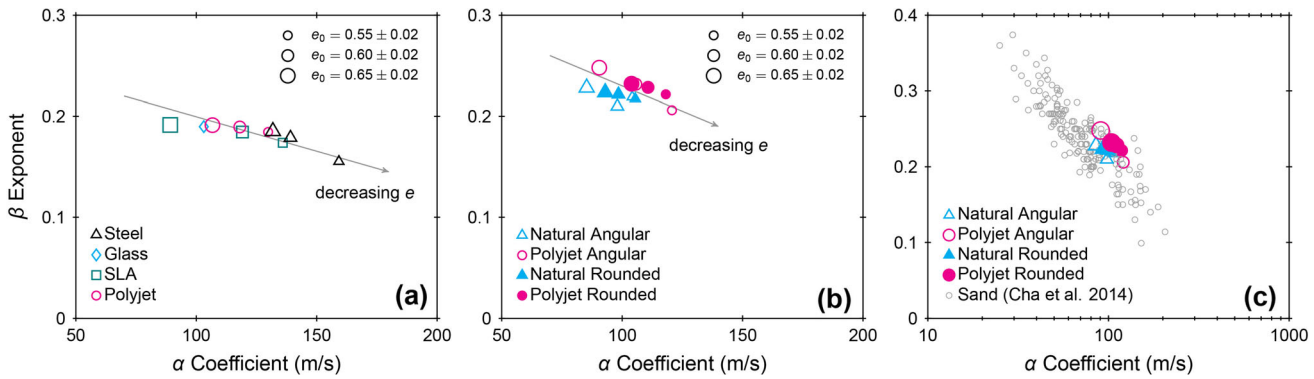

Fig. 18 β-exponent versus α-coefficient for specimens of **a** spheres, **b** angular and rounded natural particles, and **c** comparison of β-exponent versus α-coefficient with values from the literature

The steel spheres exhibit significantly higher G_{max} compared to other materials due to the greater stiffness and density of steel. Both types of AM spheres exhibit similar G_{max}, which are smaller than those for glass. Figure 19d–f presents G_{max} measurements for specimens of angular and rounded natural and AM particles, which increase with decreasing e_0 and increasing p', similar to the spherical specimens. The natural particles exhibit higher G_{max} compared to the AM particles due to the sand specimens' greater density. Also, both the natural and AM rounded particles had larger G_{max} values than the angular particles.

The shear modulus of a particle assembly under an effective isotropic stress, σ′, can be represented by the following power equation [25]:

$$G_{max} = \mathrm{AF}(e)(p')^n \tag{8}$$

where A is a coefficient that depends on the fabric and the constituent materials' elastic properties, F(e) is a function

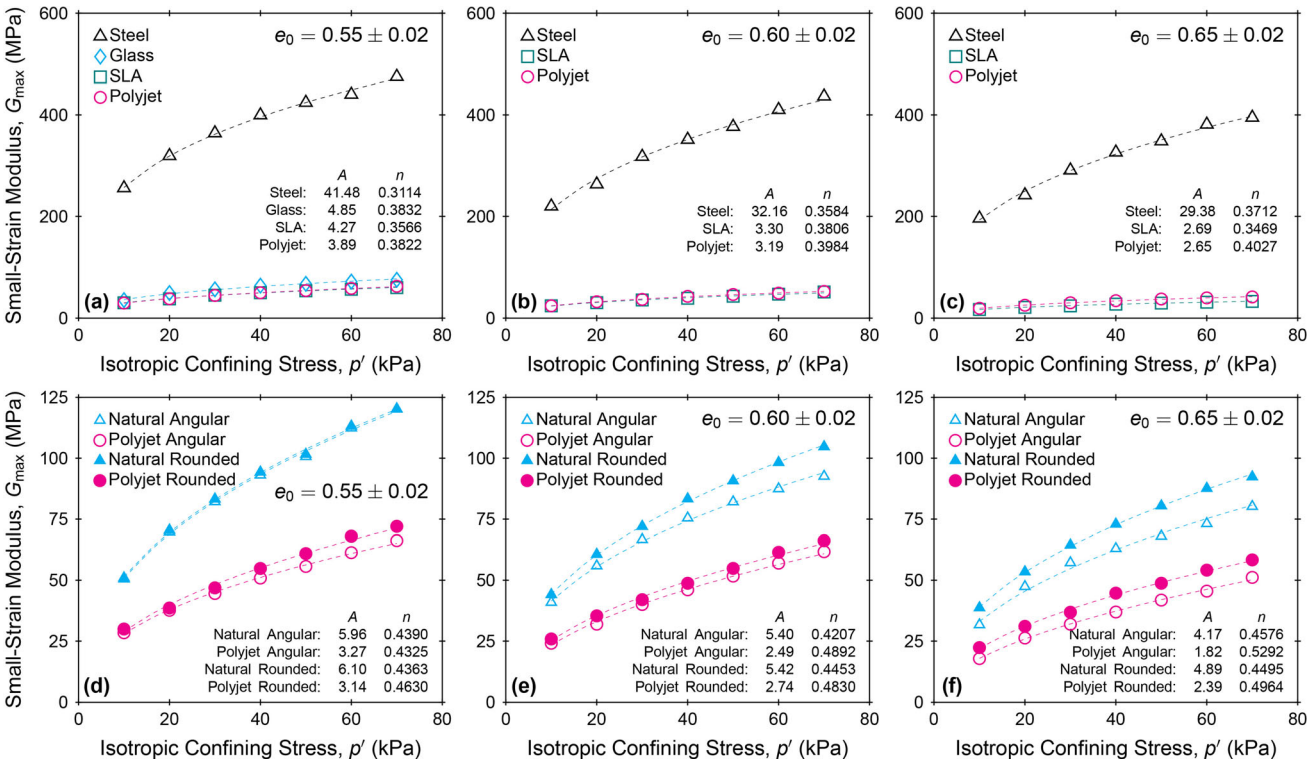

Fig. 19 Small-strain moduli for specimens of **a**, **b**, **c** spheres and **d**, **e**, **f** angular and rounded natural and additive manufactured particles

of the void ratio, and n is an exponent that describes the sensitivity of G_{max} to changes in p'. The parameters A, $F(e)$, and n can be determined empirically [24, 25] or analytically for an assembly with an isotropic stress state using Hertz contact theory or rough contact theory [14, 54].

Figure 20a, b shows the values of A-coefficients and n-exponents for the sphere and sand particle specimens, respectively. In the same manner as the results shown in Fig. 18a, b, the A-coefficients generally increase as e_0 is decreased. Relative to the other sphere specimens, the steel spheres have significantly higher A-coefficients and the AM spheres have the smallest. The n-exponents for all spheres range between 0.3114 and 0.4027, with the smaller values of the range representing the steel sphere specimens and the larger values representing the AM sphere specimens. The A-coefficients for the natural particle specimens are larger than those for the analog particle specimens, and the n-exponents range between 0.421 and 0.458 for natural sand and between 0.432 and 0.529 for analog sand. These values are in agreement with those reported in the literature [16, 24]. These observations also indicate that the SLA and

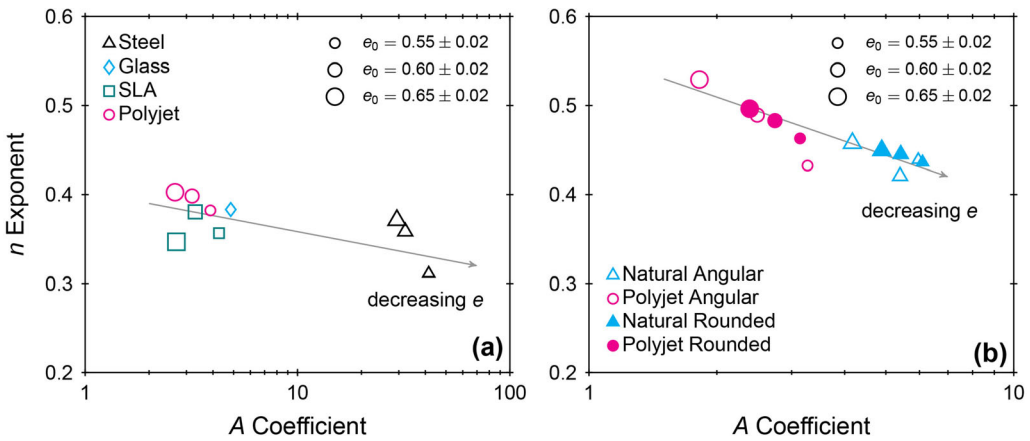

Fig. 20 n-exponent versus A-coefficient for specimens of **a** spheres and **b** angular and rounded natural and additive manufactured particles

polyjet analog particles can be used to model the relationship between G_{max} and p' for coarse-grained soils.

6 Implication on experimental and numerical studies

The results presented in this paper highlight several aspects of both the SLA and polyjet additive manufacturing technologies related to the ability of AM analogs to model the behavior of natural soils. Both the SLA and polyjet technologies have their own advantages and limitations. From a manufacturing perspective, polyjet technology is better equipped to successfully and more efficiently reproduce the shape of natural sand particles (Figs. 6, 7). This is because the support structure in polyjet AM is composed of a gel-like material that does not alter the surface of the 3D printed particles. SLA technology, on the other hand, requires solid support structures that must be removed from each individual particle, resulting in a slower production and an asperity on the particle surface (Fig. 5).

From a modeling perspective, the contact deformation response of SLA particles was similar to that of glass, which is typically used as an analog for quartz particles (Fig. 10a). In comparison, the polyjet spheres accumulated larger contact plastic deformations (Fig. 10a), likely due to the significantly larger surface roughness produced by the printing procedure (Figs. 5, 6). The 1D compression response of assemblies of AM particles suggests that normalization of the applied stresses by the constituent material stiffness may provide a viable framework for modeling the compression behavior. However, assemblies of spherical and analog sand polyjet particles indicate that their compressibility is larger than that of assemblies of glass and natural soil particles, likely due to plastic deformation of the polyjet particles' micro-asperities (Figs. 11, 12, 13, 14). Shear wave velocity and shear modulus measurements indicate that the AM analogs have a similar dependency on mean effective stress as natural sands, suggesting that this behavior is appropriately modeled by the analogs (Figs. 18, 20).

The results presented herein highlight the potential benefits that additive manufacturing technology can provide for the study of the behavior of granular materials. Possibly, the greatest advantage of the AM technology is the ability to systematically control individual particle properties, such as particle size, shape, and constituent material stiffness. In addition, as pointed out by Kittu et al. [32], AM particle analogs may enhance validation procedures for DEM models against experimental data. Namely, use of AM could ensure that the same particle shape and sizes are being tested in both numerical and experimental tests. However, this requires DEM models to accurately capture the normal and shear force–displacement response of the AM material, which can deviate from Hertz theory for materials such as the polyjet polymer.

7 Conclusions

This paper provides the results of an investigation into the feasibility of using additive manufacturing technology to generate particle analogs to model the mechanical behavior of coarse-grained soils. The behaviors investigated include uniaxial inter-particle compression, oedometric compression, and shear wave transmission. The materials tested were stainless steel, borosilicate glass, and SLA and polyjet AM spheres, as well as natural and AM sand particles. The main findings are summarized as follows:

- AM technologies can accurately reproduce the shape of natural coarse sand particles. However, the surface texture of the AM particles is determined by the specific manufacturing procedure, resulting in different surface roughnesses that can affect the inter-particle contact behavior.
- The results from uniaxial inter-particle compression tests on spheres of different constituent materials indicate that the contact normal force–displacement response of the SLA AM particles can closely model the contact behavior of glass particles using a Hertz-based normalization where the contact force is scaled by the material Young's modulus (F/E^*). However, the contact response of the polyjet particles was significantly influenced by the deformation of micro-asperities at small loads, which led to an initially softer response. The contact force at which the micro-asperities are fully deformed (N_{GT}) is larger for the polyjet particles than the SLA particles due to the larger surface roughness of the former.
- The results from oedometer tests indicate that compressive stress–strain response is influenced by the constituent material stiffness, yielding at inter-particle contacts, and densification caused by particle rearrangements. Overall, the results indicate that the 1D compression behavior can be modeled more accurately with the SLA particles with a modified Hertz-based normalization. However, the polyjet method offers the ability to reproduce a wider range of particle shapes.
- Shear wave velocity and shear modulus measurements obtained with bender elements indicate that the dependency with mean effective stress for the AM materials is similar to that of natural sands. This is confirmed by measurements on assemblies of steel, glass, and AM SLA and polyjet spheres, as well as natural and polyjet rounded and angular sand particles.

Additive manufacturing technology is rapidly evolving. Manufacturing processes are becoming faster and more precise, allowing for better representation of particle shapes. In addition, new materials are being developed, some of which have properties that are closer to natural minerals such as quartz. While the technology is readily available to manufacture analog sand particles, there is a need to carefully evaluate each manufacturing process and material for its ability to model the behavior of natural soils.

Acknowledgements This material is based upon work supported in part by the National Science Foundation (NSF) under Award No. 1735732. Any opinions, findings, and conclusions or recommendations expressed in this material are those of the author(s) and do not necessarily reflect those of the NSF.

References

1. Adamidis O, Alber S, Anastasopoulos I (2020) Assessment of three-dimensional printing of granular media for geotechnical applications. Geotech Test J. https://doi.org/10.1520/GTJ20180259
2. Ahmed SS, Singh M, Martinez A (2019) Particle-scale contact response of 3D printed particle analogs. In: Engineering mechanics institute conference. Pasadena, CA
3. Altuhafi FN, Coop MR, Georgiannou VN (2016) Effect of particle shape on the mechanical behavior of natural sands. J Geotech Geoenviron Eng 142:1–65. https://doi.org/10.1061/(ASCE)GT.1943-5606.0001569
4. Antonyuk S, Tomas J, Heinrich S, Mörl L (2005) Breakage behaviour of spherical granulates by compression. Chem Eng Sci 60:4031–4044. https://doi.org/10.1016/j.ces.2005.02.038
5. Athanassiadis AG, Miskin MZ, Kaplan P et al (2014) Particle shape effects on the stress response of granular packings. Soft Matter 10:48–59. https://doi.org/10.1039/c3sm52047a
6. Bartake PP, Singh DN (2007) Studies on the determination of shear wave velocity in sands. Geomech Geoeng 2:41–49. https://doi.org/10.1080/17486020601065449
7. Bui MT (2009) Influence of some particle characteristics on the small strain response of granular materials. University of Southampton, School of Civil Engineering and the Environment, Doctoral Thesis, 252pp
8. Cascante G, Santamarina JC (1996) Interparticle contact behavior and wave propagation. J Geotech Geoenviron Eng 122:831–839
9. Casini F, Brauchli S, Herzog R, Springman SM (2011) Grain size distribution and particle shape effects on shear strength of sand–gravel mixtures. In: 15th European conference on soil mechanics and geotechnical engineering hard soils-weak rocks, pp 149–154. https://doi.org/10.3233/978-1-60750-801-4-149
10. Cavarretta I, Coop M, O'Sullivan C (2010) The influence of particle characteristics on the behaviour of coarse grained soils. Geotechnique 60:413–423. https://doi.org/10.1680/geot.2010.60.6.413
11. Cavarretta I, O'Sullivan C, Ibraim E et al (2012) Characterization of artificial spherical particles for DEM validation studies. Particuology 10:209–220. https://doi.org/10.1016/j.partic.2011.10.007
12. Cavarretta I, O'Sullivan C, Coop MR (2017) The relevance of roundness to the crushing strength of granular materials. Geotechnique 67:301–312. https://doi.org/10.1680/jgeot.15.P.226
13. Cha M, Santamarina JC, Kim HS, Cho GC (2014) Small-strain stiffness, shear-wave velocity, and soil compressibility. J Geotech Geoenviron Eng 140:1–4. https://doi.org/10.1061/(ASCE)GT.1943-5606.0001157
14. Chang CS, Misra A, Sundaram SS (1991) Properties of granular packings under low amplitude cyclic loading. Soil Dyn Earthq Eng 10:201–211. https://doi.org/10.1016/0267-7261(91)90034-W
15. Cho GC, Dodds J, Santamarina JC (2006) Particle shape effects on packing density, stiffness, and strength: natural and crushed sands. J Geotech Geoenviron Eng 132:591–602. https://doi.org/10.1061/(ASCE)1090-0241(2006)132:5(591)
16. Chung R, Yokel F, Drnevich V (1984) Evaluation of dynamic properties of sands by resonant column testing. Geotech Test J 7:60–69. https://doi.org/10.1520/gtj10594j
17. Cole DM, Peters JF (2007) A physically based approach to granular media mechanics: grain-scale experiments, initial results and implications to numerical modeling. Granul Matter 9:309–321. https://doi.org/10.1007/s10035-007-0046-2
18. Cole DM, Peters JF (2008) Grain-scale mechanics of geologic materials and lunar simulants under normal loading. Granul Matter 10:171–185. https://doi.org/10.1007/s10035-007-0066-y
19. Goldsmith W, Lyman PT (1960) The penetration of hard-steel spheres into plane metal surfaces. J Appl Mech Trans ASME 27:717–725. https://doi.org/10.1115/1.3644088
20. Greenwood JA, Tripp JH (1964) The elastic contact of rough spheres. J Appl Mech Trans ASME 34:153–159. https://doi.org/10.1115/1.3607616
21. Guida G, Viggiani GMB, Casini F (2019) Multi-scale morphological descriptors from the fractal analysis of particle contour. Acta Geotech 15:1067–1080. https://doi.org/10.1007/s11440-019-00772-3
22. Gupta R, Salager S, Wang K, Sun WC (2019) Open-source support toward validating and falsifying discrete mechanics models using synthetic granular materials—Part I: experimental tests with particles manufactured by a 3D printer. Acta Geotech 14:923–937. https://doi.org/10.1007/s11440-018-0703-0
23. Hanaor DAH, Gan Y, Revay M et al (2016) 3D printable geomaterials. Geotechnique 66:323–332. https://doi.org/10.1680/jgeot.15.P.034
24. Hardin BO, Black WL (1966) Sand stiffness under various triaxial stresses. J Soil Mech Found Div 92:27–42
25. Hardin BO, Richart F Jr (1963) Elastic wave velocities in granular soils. J Soil Mech Found Div 89:33–654
26. Islam MN, Siddika A, Hossain MB et al (2011) Effect of particle size on the shear strength behaviour of sands. Aust Geomech J 46:85–95
27. Iwasaki T, Tatsuoka F (1977) Effects of grain size and grading on dynamic shear moduli of sands. Soils Found 17:19–35
28. Jiménez M, Romero L, Domínguez IA et al (2019) Additive manufacturing technologies: an overview about 3D printing methods and future prospects. Complexity. https://doi.org/10.1155/2019/9656938
29. Kagami J, Yamada K, Hatazawa T (1983) Contact between a sphere and rough plates. Wear 87:93–105. https://doi.org/10.1016/0043-1648(83)90025-X
30. Kara EM, Megachou M, Aboubekr N (2013) Contribution of particles size ranges to sand friction. Eng Technol Appl Sci Res 3:497–501
31. Kirkpatrick WM (1965) Effects of grain size and grading on the shearing behavior of granular materials. Sixth Int Conf Soil Mech Found Eng 1:273–277
32. Kittu A, Watters M, Cavarretta I, Bernhardt-Barry ML (2019) Characterization of additive manufactured particles for DEM validation studies. Granul Matter 21:1–15. https://doi.org/10.1007/s10035-019-0908-4

33. Liu X, Yang J (2018) Shear wave velocity in sand: effect of grain shape. Geotechnique 68:742–748. https://doi.org/10.1680/jgeot.17.T.011
34. Marschi ND, Chan CK, Seed HB (1972) Evaluation of properties of rockfill materials. ASCE J Soil Mech Found Div 98:95–114
35. Matsumura S, Kobayashi T, Mizutani T, Bathurst RJ (2017) Manufacture of bonded granular soil using X-ray CT scanning and 3D printing. Geotech Test J 40:1000–1010. https://doi.org/10.1520/GTJ20160273
36. Miskin MZ, Jaeger HM (2013) Adapting granular materials through artificial evolution. Nat Mater 12:326–331. https://doi.org/10.1038/nmat3543
37. Mitchell JK, Soga K (2005) Fundamentals of soil behavior, 3rd edn. Wiley, New York
38. Miura K, Maeda K, Toki S (1997) Method of measurement for the angle of repose of sands. Soils Found 37:89–96
39. Najmon JC, Raeisi S, Tovar A (2019) Review of additive manufacturing technologies and applications in the aerospace industry. Elsevier, Amsterdam
40. Ngo TD, Kashani A, Imbalzano G et al (2018) Additive manufacturing (3D printing): a review of materials, methods, applications and challenges. Compos Part B Eng 143:172–196. https://doi.org/10.1016/j.compositesb.2018.02.012
41. Otsubo M, O'sullivan C, Sim WW, Ibraim E (2015) Quantitative assessment of the influence of surface roughness on soil stiffness. Geotechnique 65:694–700. https://doi.org/10.1680/geot.14.T.028
42. Patel A, Bartake PP, Singh DN (2009) An empirical relationship for determining shear wave velocity in granular materials accounting for grain morphology. Geotech Test J 32:1–10
43. Santamarina JC (2003) Soil behavior at the microscale: particle forces. In: Proceedings of a symposium on soil behavior and soft ground construction in honor of Charles C. Ladd, pp 25–56
44. Santamarina JC, Klein KA, Fam MA (2001) Soils and waves: particulate materials behavior, characterization and process monitoring. Wiley, Hoboken
45. Sharifipour M, Dano C, Hicher P (2004) Wave velocities in assemblies of glass beads using bender-extender elements. In: 17th ASCE engineering, pp 1–8
46. Tofail SAM, Koumoulos EP, Bandyopadhyay A et al (2018) Additive manufacturing: scientific and technological challenges, market uptake and opportunities. Mater Today 21:22–37. https://doi.org/10.1016/j.mattod.2017.07.001
47. Vangla P, Latha GM (2015) Influence of particle size on the friction and interfacial shear strength of sands of similar morphology. Int J Geosynth Gr Eng. https://doi.org/10.1007/s40891-014-0008-9
48. Wadell H (1932) Volume, shape, and roundness of rock particles. J Geol 40:443–451
49. Wang JJ, Zhang HP, Tang SC, Liang Y (2013) Effects of particle size distribution on shear strength of accumulation soil. J Geotech Geoenviron Eng 139:1968–1972. https://doi.org/10.1061/(ASCE)GT.1943-5606.0000931
50. Wichtmann T, Triantafyllidis T (2009) Influence of the grain-size distribution curve of quartz sand on the small strain shear modulus Gmax. J Geotech Geoenviron Eng 135:1404–1418. https://doi.org/10.1061/(ASCE)GT.1943-5606.0000096
51. Xiao Y, Long L, Evans TM et al (2019) Effect of particle shape on stress-dilatancy responses of medium-dense sands. J Geotech Geoenviron Eng 145:1–15. https://doi.org/10.1061/(ASCE)GT.1943-5606.0001994
52. Yamashita S, Kawaguchi T, Nakata Y et al (2009) Interpretation of international parallel test on the measurement of G max using bender elements. Soils Found 49:631–650. https://doi.org/10.3208/sandf.49.631
53. Yang J, Gu XQ (2013) Shear stiffness of granular material at small strains: Does it depend on grain size? Geotechnique 63:165–179. https://doi.org/10.1680/geot.11.P.083
54. Yimsiri S, Soga K (2000) Micromechanics-based stress-strain behaviour of soils at small strains. Geotechnique 50:559–571. https://doi.org/10.1680/geot.2000.50.5.559
55. Zheng J, Hryciw RD (2015) Traditional soil particle sphericity, roundness and surface roughness by computational geometry. Geotechnique 65:494–506. https://doi.org/10.1680/geot.14.P.192